Effect of particle injection on heat transfer in rotating Rayleigh-Bénard convection

Pranav Joshi,* Hadi Rajaei, Rudie P. J. Kunnen, and Herman J. H. Clercx
Fluid Dynamics Laboratory, Department of Applied Physics and J. M. Burgers Center for Fluid Dynamics, Eindhoven University of Technology, P.O. Box 513, 5600 MB Eindhoven, The Netherlands
(Received 15 March 2016; published 29 December 2016)

The present study attempts to change the regime transitions and heat transfer properties in rotating Rayleigh-Bénard convection by injecting ∼100-μm-diam particles in the flow. The particles start settling out of the fluid immediately after injection and separate entirely from the fluid over a period of several hours. The particles deposit on the top and bottom surfaces, forming porous layers with nonideal thermal properties, and, as expected, decrease the heat flux. The reduction in heat transfer is a result of the inability of the layers to respond rapidly enough to fluid temperature fluctuations. However, in the rotation-dominated geostrophic regime, the heat transfer normalized by its nonrotating value is higher in the presence of the particle layers than without them. Direct numerical simulations with ideal heat transfer walls indicate that the temperature fluctuations in the bulk become slower under the damping effect of rotation, in contrast with those in the boundary layers, which do not show any damping until the flow transitions to the geostrophic regime. In this regime, the dominant time scale of the near-wall fluid temperature fluctuations increases substantially as the rotation rate is increased. It is thus likely that the time response of the particle layers in relation to that of the nearby fluid improves only in the geostrophic regime, which is reflected in a relatively larger heat transfer.

DOI: 10.1103/PhysRevFluids.1.084301

I. INTRODUCTION

Rayleigh-Bénard convection (RBC), the flow between a heated horizontal bottom plate and a cooled parallel top plate, is a canonical system to study buoyancy driven flows. The effect of rotation along an axis normal to the plates has been the focus of numerous studies (e.g., [1–23]) as many convective flows in nature [24] and industrial processes [25] are subjected to the effects of rotation. The relevant nondimensional parameters for this system are the Rayleigh, Prandtl, and Rossby numbers, defined as, respectively,

$$\mathrm{Ra} = \frac{g\alpha\Delta T H^3}{\nu\kappa}, \tag{1}$$

$$\mathrm{Pr} = \frac{\nu}{\kappa}, \tag{2}$$

and

$$\mathrm{Ro} = \frac{\sqrt{g\alpha\Delta T/H}}{2\Omega}, \tag{3}$$

where α, ν, and κ are the isobaric thermal expansion coefficient, kinematic viscosity, and thermal diffusivity of the fluid, ΔT is the temperature difference between ideal isothermal bottom and top plates maintained at temperatures T_{bottom} and T_{top}, respectively, and a distance H apart, Ω is the

*Present address: Experimental Aerodynamics Division, National Aerospace Laboratories, Bangalore 560 017, India; jpranavr@gmail.com

angular velocity, and g is the gravitational acceleration. The parameter representing the system geometry is the aspect ratio, which for a cylindrical system is defined as

$$\Gamma = D/H, \tag{4}$$

where D is the diameter of the cylinder. The response of the Rayleigh-Bénard (RB) system to the imposed buoyancy forcing is represented by the Nusselt number

$$\mathrm{Nu} = \frac{qH}{\Delta T \lambda}, \tag{5}$$

where q is the heat flux through the system and λ is the thermal conductivity of the fluid.

The Rayleigh-Bénard system is well known for exhibiting a multitude of flow regimes and transitions between them, depending on the system parameters. Relevant to the present study, rotating Rayleigh-Bénard convection (RRBC) at moderately high Ra and Pr $\sim O(10)$ shows three turbulent regimes depending on Ro [26]: regime I (Ro $\gtrsim$ 2.5), dominated by the large-scale circulation (LSC) with negligible effects of rotation; regime II (0.1 $\lesssim$ Ro $\lesssim$ 2.5), where LSC is replaced by increasingly dominant columnar vortical plumes; and regime III, also known as the geostrophic regime (Ro $\lesssim$ 0.1), where the vortical columns span the entire height of the cell and turbulence is strongly damped by rotation. The precise values of Ro at transitions between these regimes depend on Ra, Pr, and Γ. The changes in the flow structure also result in corresponding changes in the heat transfer. The Nusselt number in regime I is indistinguishable from its nonrotating value. In regime II, as Ro decreases, Nu rises steadily and reaches a peak at the transition to regime III. This increase in heat transfer has been attributed to the mechanism of Ekman pumping [2,3,8], which draws out more fluid from the boundary layers by virtue of the radial pressure gradients imposed on them by cyclonic vortices emanating from the top and bottom plates. The heat transfer decays as Ro is further decreased in the geostrophic regime, presumably due to the increasing damping effect of rotation on the turbulence [4,17,26].

Modifying the flow structure in rotating convection, and hence the heat transfer, or tuning the locations of regime transitions in the parameter space is potentially useful in many technological applications. Such changes in the flow could be induced by means of flow additives or by modifying the boundary conditions. In the present study, we perturb the flow by introducing near-neutrally-buoyant microparticles in it and study its effect on the heat transfer. Most of the previous studies that have tested the effect of particles have done so for nonrotating convection. Many studies have focused on convection in nanofluids, but have found contradictory results for the effects of nanoparticles on the heat transfer; see, e.g., [27]. Researchers have also studied natural convection in the presence of microparticles, but most of them have reported on the particle sedimentation characteristics, e.g., [28], and the dynamics of particle layers when in suspension, e.g., [29,30], but not on the heat transfer. Their results indicate that convection can lead to particle segregation, which in turn can affect the flow dynamics.

The particle behavior can also be influenced by the Ekman pumping mechanism under system rotation. In the present work we introduce microparticles in rotating RBC in an attempt to change the flow structure and possibly shift the regime transitions in the Ro space. To assess the impact of the particles on the flow, and the heat transfer properties in particular, we use Nu as the diagnostic. To enable steady-state Nu measurements, the particles are selected to be near-neutrally buoyant aimed at maximizing the time they remain in suspension, aided by the Ekman pumping mechanism. However, we observe that the particles do not form a stable suspension and start settling out of the fluid immediately following injection, forming fluidized particle layers on the heat transfer surfaces. These layers have a low thermal conductivity (details follow in Sec. III A), i.e., nonideal heat transfer properties, and as such, decrease the heat flux. This decrease in the heat transfer is a result of the finite response time of the layers to fluid temperature fluctuations and hence also depends on the relation between the time scale of the flow and the relaxation time scale of the particle layers. As the flow time scales change with Ro, the effect of the layers on the heat transfer also varies with rotation.

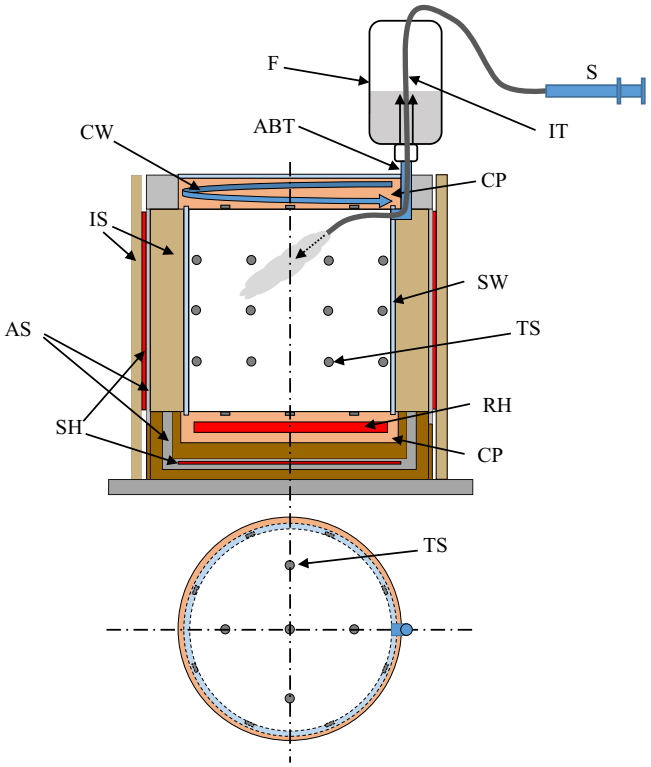

FIG. 1. Schematic of the experimental setup: SW, cylindrical Plexiglas sidewall; CP, top and bottom copper plates; RH, heating resistors fitted into the bottom CP; CW, cooling water recirculating through the top CP; ABT, air-bleed tube; SH, secondary heaters; AS, aluminium adiabatic shields; IS, insulating shields; TS, temperature sensors; IT, injection tube; F, overhead flask; and S, syringe.

We describe the measurement setup and procedures in the next section. In Sec. III we discuss the reduction in Nu under rotating and nonrotating conditions as a result of the greater thermal resistance of the particle layers and also the higher deviations of Nu in the geostrophic regime from its nonrotating values in the presence of particle layers. In Sec. IV we discuss the interplay between the time scales of the particle layers and the near-wall flow that determines the impact of the layers on the heat transfer.

II. EXPERIMENTAL SETUP AND MEASUREMENT PROCEDURES

Experiments have been performed using the Rayleigh-Bénard setup described in detail in Ref. [31], a schematic of which is shown in Fig. 1 (not to scale). The cell is 250 mm tall and has an aspect ratio $\Gamma = 1$. The cylindrical Plexiglas sidewall is 10 mm thick and is bounded by 30-mm-thick copper plates at the top and bottom. The bottom copper plate is heated by using two 12.3-Ω resistors fitted into spiral grooves within it, while the top plate is cooled by recirculating cooling water through similar grooves machined in it. The sidewall is provided with an air-bleed tube close to the top plate to facilitate the removal of air bubbles. The secondary heaters are controlled to maintain the aluminium adiabatic shields at the same temperatures as the mean temperatures of the corresponding surfaces of the RB cell. Together with the insulating shields, they minimize heat loss to the surroundings. Water is used as the working fluid. The entire setup is enclosed in a wooden box which is lined on the inside by an insulating material and mounted on a rotating table. Five thermistors are provided in each of the plates, 0.7 mm from the wetted surface. The sidewall

contains 24 sensors mounted 0.5 mm from the inner surface in three rings of eight equispaced sensors each, located at elevations $0.25H$, $0.5H$, and $0.75H$ from the bottom surface of the cell. The thermistors are calibrated with logarithmic polynomial fits and measure temperature with an accuracy of ± 0.01 °C.

The choice of particles is primarily dictated by the requirement of near-neutral buoyancy with the intention of giving reasonably stable suspensions to enable steady-state measurement of Nu. To achieve maximum thermal conductivity with near-neutral buoyancy, we opt for silver-coated hollow ceramic spheres. Since the settling velocity of particles with density ρ_p and radius r in a fluid of density ρ is proportional to $(\rho_p - \rho)r^2$, a larger particle size exacerbates the effects of density mismatch leading to higher settling and rise velocities. However, too small a particle size limits the thickness, and hence the thermal conductivity, of the silver coating. As a compromise, we use AGSL-150-30-TRD particles from Potters Industries, which have a mean density $\rho_p \approx 1.1$ g/cm^3, diameter $d_p \approx 100$ μm, and a 450-nm-thick silver coating. Attempts to manufacture particles with thicker silver layers and reasonably narrow density range proved difficult and prohibitively expensive. Successive density-based segregations using solutions of glycerin and isopropyl alcohol in water are employed to extract particles with density $0.96 \lesssim \rho_p \lesssim 1.04$ g/cm^3, which are used in the present experiments. This particular density range is selected to achieve a balance between the requirements of reasonable cost and neutral buoyancy to achieve stable suspensions. Our observations suggest that any moderately narrower density range will not alter the transient response of the system qualitatively (to be discussed in the following sections) and the steady-state response quantitatively.

The injection process utilizes a syringe, a syringe pump from ProSense B.V. (Model No. NE-4000), and an injection tube with an inner diameter of 1.5 mm. The tube is passed through the overhead flask and inserted into the cell through the air-bleed tube. The extracted particles are mixed with water at $T_{\text{mean}} = (T_{\text{top}} + T_{\text{bottom}})/2$ and injected into the cell after the flow has reached equilibrium with the injection tube inside the RB cell. The tube is removed immediately after injection is completed. Care is exercised to ensure that no air bubbles are introduced in the cell during the injection process. Water displaced from the RB cell by the injected fluid is collected in the overhead flask. An injection rate of 50 ml/min is employed, resulting in an injection velocity of 0.47 m/s, which is non-negligible. However, preliminary tests for injection of water without particles show no measurable impact of the injection on Nu.

Measurement variables include the temperatures of the top and bottom plates and the sidewall, as well as the input heat flux to the bottom plate q_I. Data are recorded at a sampling frequency of 1 Hz and averaged over a period of 6 h or longer under steady state. Temperatures recorded by the five sensors in the top (bottom) plate are averaged to calculate the mean top (bottom) plate temperature, while fluid properties are evaluated at T_{mean}. No correction for the finite conductivity of the copper plates has been applied. A set of measurements has been performed with top and bottom plates maintained at the same temperature T_0 for different values of T_0 to measure the loss of heat to the surroundings from the lower plate $q_L(T_0)$. The corrected values $q = q_I - q_L$ have been used in Eq. (5) to calculate Nu. All measurements reported in this paper have been performed at $T_{\text{mean}} = 24.1$ °C (Pr $= 6.4$) and using particle volume fraction $0.02\% \leqslant \phi \leqslant 1\%$. Relevant measurement parameters for all the experiments are included in Table I.

III. RESULTS

A. Particle injection without rotation

The response of the RB system to particle injection has been first tested without rotation at Ra $= 2.2 \times 10^9$ and a particle volume fraction $\phi = 0.09\%$ (run PnR2). The flow is allowed to reach equilibrium prior to the injection of particles. Figure 2 shows the variation of the heat flux with time during the experiment. The injection period is indicated by the two vertical dashed lines. It is evident that the heat flux starts decreasing immediately after the injection begins and continues to decrease for 3–4 h before reaching a new statistically steady state.

TABLE I. Parameters for all the experiments. The nomenclature of the runs uses P for particles, R for rotation, and the prefix n for negation. For example, nPR3 denotes an experiment with rotation and no particles. For the runs in which the nominal Rayleigh number Ra_n is varied, i.e., nPnR, PnR1, PnR2, PnR3, and PnR4, the minimum and maximum values of ΔT, Ra_n, and δT (not for nPnR) are specified. For the runs in which Ro is varied at a nominally constant Ra_n, i.e., runs nPR1, nPR2, nPR3, PR1, PR2, and PR3, variations in Ra_n from the listed values are within approximately 1%. Deviations of T_{mean} from its listed values for all the runs are typically less than 0.1 °C. The large variations in $\mathrm{Ra}_{\mathrm{layer}}$ reflect the variations in the particle layer temperature between top and bottom plates and for different Ra_n. The values of e, ϕ_{layer}, κ_{layer}, and $\mathrm{Ra}_{\mathrm{layer}}$ have not been included for runs PnR1 and PR1 due to high uncertainty in e. Estimates for κ_{layer} use λ_{layer} values that have been estimated using Eqs. (8) and (9) (also see Fig. 5).

Run	ΔT (°C)	T_{mean} (°C)	$\mathrm{Ra}_n \times 10^{-9}$	Ro_n	$\phi \times 10^2$	e (mm)	$\phi_{\mathrm{layer}} \times 10^2$	$\kappa_{\mathrm{layer}} \times 10^6$ (m^2/s)	δT (°C)	$\mathrm{Ra}_{\mathrm{layer}} \times 10^4$
nPnR	2.00–30.38	24.24	0.58–8.97	∞	0	0	0			
nPR1	2.86	24.11	0.83	0.05–4.74	0	0	0			
nPR2	4.91	24.15	1.43	0.05–4.01	0	0	0			
nPR3	7.70	24.11	2.23	0.07–3.99	0	0	0			
PnR1	7.37–7.77	24.08	2.13–2.24	∞	0.023				0.155–0.159	
PnR2	2.00–31.06	24.09	0.58–9.03	∞	0.09	0.75	15.0	1.06	0.06–1.77	2.3–123
PnR3	2.00–31.44	24.06	0.58–9.04	∞	0.22	1	27.5	1.43	0.09–2.47	0.53–31.1
PnR4	2.04–31.71	24.09	0.59–9.14	∞	1.01	4	31.6	1.55	0.24–6.04	3.4–167.8
PR1	7.71	24.11	2.23	0.07–5.00	0.023				0.16–0.18	
PR2	7.81	24.07	2.25	0.07–5.04	0.22	1	27.5	1.43	0.47–0.51	1.8–2.8
PR3	7.90	24.06	2.28	0.07–5.08	1.01	4	31.6	1.55	1.19–1.29	11.5–17.3

The decrease in the heat flux is caused by the settling of particles on the horizontal heat transfer surfaces. The injected particles ($\sim$100 μm) are significantly smaller than the kinematic boundary layer thickness, which, according to the Grossmann-Lohse theory [32,33], is estimated to be $\delta_v \approx$ 6 mm for $\mathrm{Ra} = 2.2 \times 10^9$ and $\mathrm{Pr} = 6.4$. Thus it is likely that the erupting plumes are not able to resuspend particles that penetrate the near-wall region, 'trapping' them in the boundary layers, and leading to the formation of particle layers on the horizontal surfaces. Visual observations during preliminary measurements without insulation (to provide optical access) indicate that the particles begin to settle on the top and bottom plates immediately after being introduced into the flow. This settling is concomitant with a decrease in the heat flux. The observed settling of the particles into layers can be expected to be faster if the density of the particles departs more from that of water. Note that although the fluid density varies over the flow domain due to the temperature fluctuations,

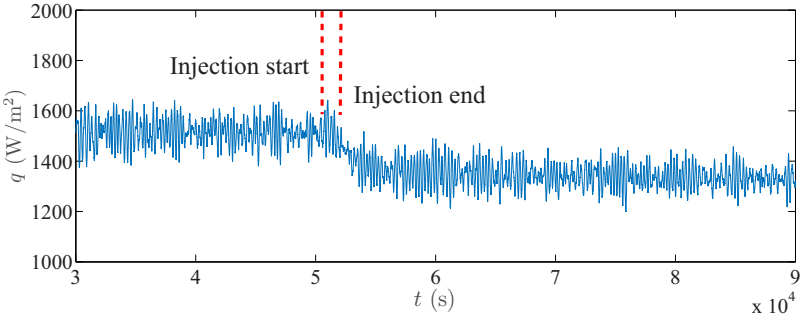

FIG. 2. Variation of heat flux with time during particle injection for run PnR2: $\phi = 0.09\%$, $\mathrm{Ra}_n = 2.2 \times 10^9$, and $1/\mathrm{Ro} = 0$.

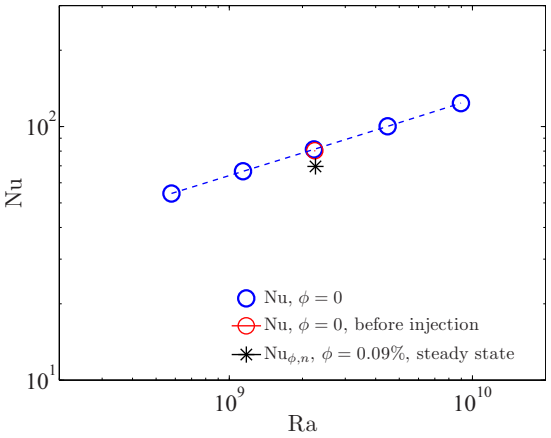

FIG. 3. Decrease in Nu as a result of particle injection for particle volume fraction $\phi = 0.09\%$ at $\mathrm{Ra}_n = 2.2 \times 10^9$ and $1/\mathrm{Ro} = 0$. Blue circles are data from run nPnR, while the red circle and black star are from run PnR2.

its variation ($\sim\pm 0.1\%$) is negligible in comparison to the spread of the particle density distribution ($\sim\pm 4\%$) and is not expected to substantially affect the settling process. Interparticle forces such as van der Waals and electrostatic forces are not expected to play an important role in the layer formation either. The average particle size (100 μm) and the interparticle distances when in suspension are too large for the attractive van der Waals force to be important in comparison to the hydrodynamic forces. The van der Waals force is active only over distances smaller than a few hundred angstroms, whereas even inside the particle layers, the interparticle surface-to-surface distances are expected to be $\sim O(20\ \mu\mathrm{m})$ (discussion of the layer porosity follows later in this section), assuming a cubic arrangement of particles. Electrostatic forces can exist between the particles suspended in water or other dielectric media [34], but are repulsive in nature, likely very small, and cannot aid the observed precipitation of particles into layers. With the current experimental setup, it is not possible for us to estimate the time variation of the fraction of particles suspended in the fluid and hence the effective thermal properties of the fluid-particle mixture and the instantaneous Nusselt number. However, since a negligible number of particles remain in suspension at the end of the period of transient heat flux, the thermal properties of the mixture can then be well represented by those of water.

In Fig. 3 we compare the nominal Nusselt number in this steady state $\mathrm{Nu}_{\phi,n} = qH/\lambda\Delta T$ with that prior to particle injection. The subscript ϕ indicates quantities measured in the presence of particle layers, while n represents nominal values, i.e., based on the nominal temperature difference ΔT applied between the copper plates and the cell height H. The figure also shows the variation of Nu with Ra for $\phi = 0$ from a separate run nPnR (see Table I) without particles. For all the results presented hereafter, uncertainties in Nu are approximately 0.2% for $\phi = 0$ and $\lesssim 0.4\%$ for $\phi \neq 0$, unless stated otherwise. The Nusselt number prior to injection in run PnR2 deviates slightly, by 1.3%, from Nu for the run nPnR due to the presence of the injection tube inside the RB cell. Evidently, the decrease in the nominal Nusselt number (or q) due to particle injection, approximately 13.2%, is two orders of magnitude larger than the particle volume fraction ($\phi = 0.09\%$) and indicates that the heat transport is highly sensitive to the presence of the particles at the heat transfer surfaces. Although not the focus of the present article, it should be noted that the high sensitivity of Nu to the presence of particles can have implications for experiments employing particles for measurement or flow visualization. If the system is allowed to stand for a period of, say, a day, i.e., with $\Delta T = 0$, and then ΔT is reapplied, the Nusselt number further decreases slightly ($<1\%$), perhaps as the small amount of particles still in suspension settle out of the fluid. As further measurements at the same Ra result in the same value for the Nusselt number (within experimental uncertainty), fresh particle injections are not carried out to measure $\mathrm{Nu}_{\phi,n}$ for varying Ra at constant ϕ.

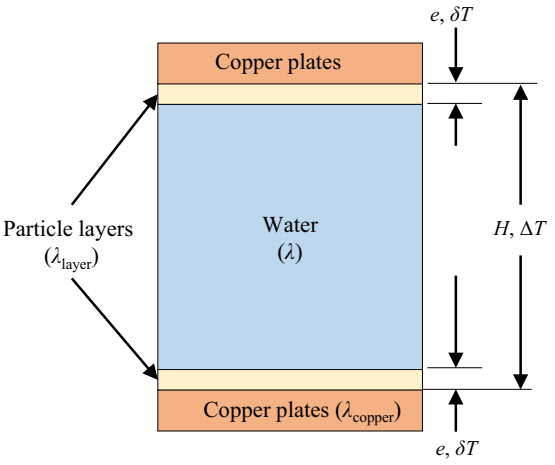

FIG. 4. Schematic showing relevant dimensions and thermal properties of copper plates and particle layers. The figure is not to scale. In particular, the thickness of the particle layers is greatly exaggerated.

The sharp decrease in the heat transfer due to the presence of the particle layers indicates that the thermal conductivity of the layers is significantly lower than that of the copper plates. To estimate the layer conductivity, we use the empirical relation for predicting the decrease in Nu due to the finite conductivity of heat transfer plates suggested by Verzicco [35] and an alternate expression proposed by Brown *et al.* [36]. The equation proposed by Verzicco [35] is

$$\frac{\mathrm{Nu_V}}{\mathrm{Nu_\infty}} = 1 - \exp[-(X_\mathrm{V}/4)^{1/3}], \tag{6}$$

with

$$X_\mathrm{V} = \frac{\lambda_\mathrm{layer}(H-2e)}{\lambda e \mathrm{Nu_V}}, \tag{7}$$

where we have treated the particle layers as plates of thickness e and conductivity λ_layer (see Fig. 4) to adapt the original relations to our purpose. In Eqs. (6) and (7) $\mathrm{Nu_V} = q(H-2e)/\Delta T\lambda$ is the Nusselt number based on the temperature difference ΔT applied between the bottom and top copper plates and the effective cell height in the presence of the particle layers $H-2e$. The ideal Nusselt number measured in the absence of particles is denoted by $\mathrm{Nu_\infty}$. We treat the copper plates as ideal infinite conductivity plates since, as will be seen shortly, $\lambda_\mathrm{layer} \ll \lambda_\mathrm{copper}$.

The equation proposed by Brown *et al.* [36] is

$$\frac{\mathrm{Nu_B}}{\mathrm{Nu_\infty}} = 1 - \exp[-(aX_\mathrm{B})^b], \tag{8}$$

with

$$X_\mathrm{B} = \frac{\lambda_\mathrm{layer}(H-2e)}{\lambda e \mathrm{Nu_B}}, \tag{9}$$

where $a = 0.378$, $b = 0.488$ for $D = 24.8$ cm, and $\Gamma = 1$. In Eqs. (8) and (9), $\mathrm{Nu_B} = q(H-2e)/(\Delta T - 2\delta T)\lambda$ is based on the effective cell height and the actual temperature difference $\Delta T - 2\delta T$ experienced by the fluid, which differs from the applied one due to the temperature drop δT across each particle layer. The treatment of particle layers as finite conductivity walls assumes that heat is transferred through the layers by conduction alone, which will be shown to be a reasonable assumption in the following paragraphs. Using Eqs. (8) and (9) [or (6) and (7)] and the measured values of e (visually) and q, we can estimate λ_layer, and hence δT, for given values of ϕ and Ra_n.

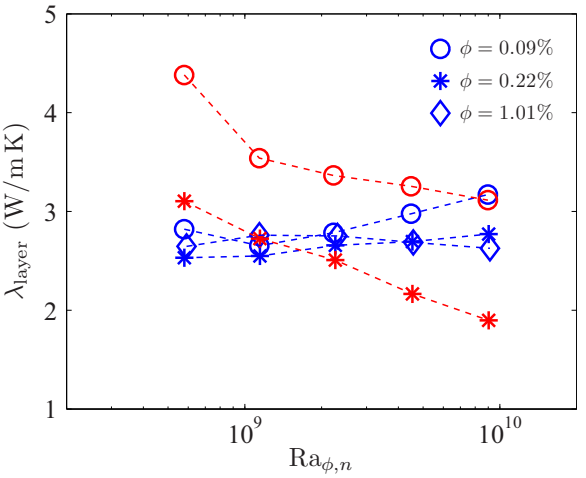

FIG. 5. Estimates of particle layer conductivities for different $\text{Ra}_{\phi,n}$ and particle volume fraction ϕ (runs PnR2, PnR3, and PnR4). Red and blue symbols represent estimates obtained using Eqs. (6) and (8), respectively. Uncertainty in λ_{layer} as a result of the estimated uncertainty in the measurement of e is typically less than $\pm 50\%$. Data for $\phi = 0.023\%$ are not shown since the layer thickness is too small to be determined with reasonable accuracy. For comparison, $\lambda_{\text{copper}} \approx 400$ W/m K at 24 °C [37].

Figure 5 shows the estimates of λ_{layer} obtained using both sets of relations for different values of Ra_n for three particle volume fractions $\phi = 0.09\%, 0.22\%$, and 1.01% (runs PnR2, PnR3, and PnR4). We do not include conductivity values for $\phi = 0.023\%$ (run PnR1) because this particle volume fraction is too low to form a uniform layer of particles on the copper plates. Estimates for $\phi = 1.01\%$ using Eq. (6) have not been included since the extremely low values of X_{V} are beyond the range of applicability of relation (6). For any constant ϕ, the use of Eqs. (6) and (8) results in variations in λ_{layer} smaller than 50% and 18%, respectively, over the range $\text{Ra}_n \approx (6 \times 10^8)$–$(9 \times 10^9)$. Since λ_{layer} can be expected to be constant for a given particle layer, it is evident that Eq. (8) performs better than Eq. (6) at estimating λ_{layer}. Note that, as mentioned earlier, λ_{layer} is significantly smaller than $\lambda_{\text{copper}} \approx 400$ W/m K [37]. The calculated particle layer conductivity is sensitive to the uncertainty in the measurement of e. The uncertainties in both e and λ_{layer} are $O(50\%)$, except for the case $\phi = 0.023\%$, in which the uncertainties are greater than 100%. However, δT, and hence the actual Nusselt number, is largely independent of e. For instance, the uncertainty in δT even for $\phi = 0.023\%$ is less than 0.5%. To show this insensitivity of δT to the uncertainty in e, we rewrite X_{B} using $\text{Nu}_{\text{B}} = q(H - 2e)/(\Delta T - 2\delta T)\lambda$ and $\lambda_{\text{layer}}/e = q/\delta T$ to get

$$X_{\text{B}} = \frac{\Delta T - 2\delta T}{q}\frac{q}{\delta T} = \frac{\Delta T - 2\delta T}{\delta T}. \tag{10}$$

Thus, X_{B}, the ratio of the thermal resistance of the fluid to that of the particle layers, is a function only of the temperature differences across the respective media. Furthermore, provided $e \ll H$ ($H = 250$ mm and $e_{\max} = 4$ mm; see Table I), $H - 2e \approx H$. Thus, it is evident that Nu_{B} also depends very weakly on e and varies only with δT. Hence, the "correct" value of δT, i.e., the one that simultaneously satisfies Eqs. (8) and (9), is independent of e and λ_{layer}. Any variation in the measured value of e results in a corresponding proportional variation in the estimated λ_{layer}, leaving $\delta T = q(e/\lambda_{\text{layer}})$ unchanged. A similar argument can be made for the insensitivity of Nu_{V} and X_{V} to e.

Once δT is known, we can calculate the actual values of Nusselt and Rayleigh numbers in the presence of particle layers as $\text{Nu}_\phi = q(H - 2e)/(\Delta T - 2\delta T)\lambda$ and $\text{Ra}_\phi = g\alpha(\Delta T - 2\delta T)(H - 2e)^3/\kappa\nu$, respectively. Figure 6 shows the variation of Nu_ϕ with Ra_ϕ for $\phi = 0.09\%$. Nominal values of Nusselt number $\text{Nu}_{\phi,n}$ are substantially lower than the ideal values ($\phi = 0$). After correcting for

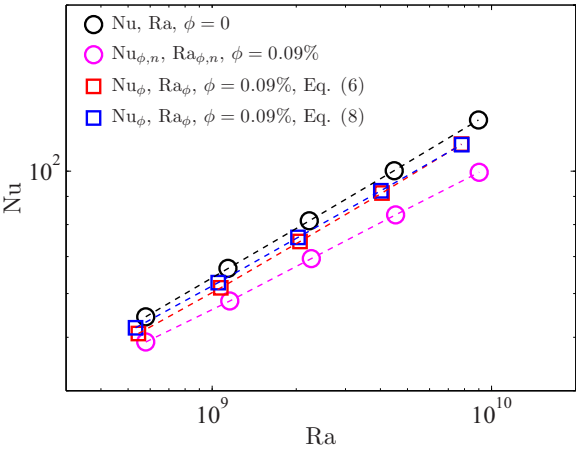

FIG. 6. Variation of Nu with Ra for particle volume fraction $\phi = 0$ (run nPnR) and Nu_{ϕ} with Ra_{ϕ} for $\phi = 0.09\%$ (run PnR2). For $\phi \neq 0$, the figure shows both nominal values $\mathrm{Nu}_{\phi,n}$ before applying correction for δT and the corrected estimates Nu_{ϕ}.

the temperature drop across the particle layers, Nu_{ϕ} estimates move closer to the ideal values, but remain lower than them, as expected [35]. Also, as the temperature difference experienced by the fluid is smaller than the imposed one, Ra_{ϕ} is lower than $\mathrm{Ra}_{\phi,n}$. Similar trends are observed for other values of ϕ (not shown). As ϕ (or e) increases for a given Ra_n, X_V and X_B decrease, resulting in higher values of $\mathrm{Nu}_{\infty} - \mathrm{Nu}_{\phi}$. A similar effect is observed as Ra_n increases for fixed ϕ. Thus, the heat transfer becomes less efficient in comparison to the ideal cases as ϕ or Ra_n increases, i.e., as the thermal resistance of the particle layer increases in comparison to that of the convecting fluid.

To justify the use of Eqs. (6) and (8) to estimate λ_{layer}, we now show that the heat transfer within the particle layers is predominantly conductive. The measurement of the layer thickness, and hence its volume, can help us estimate the particle volume fraction in the layer using the known volume of injected particles. For example, for the experiment with $\phi = 0.09\%$, the actual volume fraction of the particles inside the layer in the steady state is $\phi_{\mathrm{layer}} = \phi H/2e \approx 15\%$. Thus it can be treated as a porous medium, with permeability [38]

$$k = \frac{\epsilon^3}{150(1-\epsilon)^2} d_p^2, \tag{11}$$

where $\epsilon = 1 - \phi_{\mathrm{layer}}$ is the porosity of the layer, and hence we can calculate the porous Rayleigh number for the particle layer as [38]

$$\mathrm{Ra}_{\mathrm{layer}} = \frac{kg\alpha\Delta T e}{\kappa_{\mathrm{layer}}\nu}, \tag{12}$$

where κ_{layer} is the effective thermal diffusivity of the particle-fluid mixture in the layer. The specific heat capacity of the particle layer can be estimated from its composition ($\phi_{\mathrm{layer}} \approx 15\%$ and the fraction of Ag in particles by weight 30%) to be approximately 2580 J/kg K. Assuming $\lambda_{\mathrm{layer}} \approx 2.75$ W/m K (see Fig. 5) and density of the layer $\rho_{\mathrm{layer}} \approx 1000\,\mathrm{kg/m^3}$ results in $\kappa_{\mathrm{layer}} \approx 1 \times 10^{-6}\,\mathrm{m^2/s}$. The temperature dependence of α and ν for water leads to a significant difference between $\mathrm{Ra}_{\mathrm{layer}}$ for the top and bottom particle layers: $\mathrm{Ra}_{\mathrm{layer}}$ for $\phi = 0.09\%$ varies between 2.05×10^{-4} and 1.23×10^{-2}. The highest value of $\mathrm{Ra}_{\mathrm{layer}}$ in the present experiments is 1.7×10^{-2} for $\phi = 1.01\%$ (run PnR4; see Table I), which is substantially smaller than the critical value of $4\pi^2$ (for impermeable boundaries) [39] for the onset of convection in porous media. Thus, in the absence of any fluid flow, the heat transfer in the layers occurs only by conduction, justifying the use of Eqs. (6) and (8) to estimate their thermal conductivity. The values of ϕ, ϕ_{layer}, κ_{layer}, and $\mathrm{Ra}_{\mathrm{layer}}$ for all experiments are

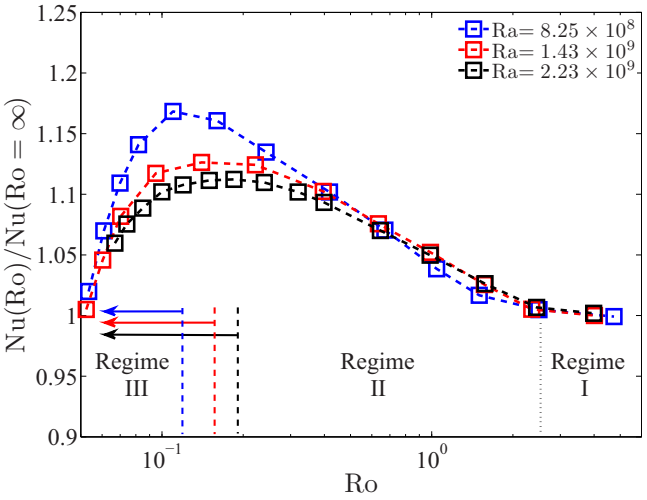

FIG. 7. Variation of Nu(Ro)/Nu(Ro $= \infty$) with Ro for particle volume fraction $\phi = 0$ and different Ra (runs nPR1, nPR2, and nPR3). The vertical black dotted line indicates the transition between regimes I and II for all Ra, while the Ro at the transition between regimes II and III for the three data sets are shown by vertical dashed lines of the corresponding colors.

presented in Table I. All the results to be presented from here on in this paper utilize Eqs. (8) and (9) to estimate λ_{layer}.

B. Particle injection under rotation

Before discussing results for particle injection under rotation, we present data for Nusselt number measurements under rotation without particles performed at Ra $= 8.3 \times 10^8$, 1.4×10^9, and 2.2×10^9. Figure 7 shows the variation of Nu normalized by its nonrotating value, with Ro. Approximate locations of transitions between different regimes are also shown by vertical dashed lines. As Ro decreases, Nu(Ro)/Nu(Ro $= \infty$) increases in regime II, reaches a peak, and then decays as Ro is further reduced in regime III. Furthermore, the increase in heat transfer under rotation is higher for lower Ra. These trends are in line with those observed for similar Pr in numerous previous studies (e.g., [6,8,13,16,26]). In the following, the data without particles are used as a benchmark to study the effects of the particle layers on the heat transfer.

For the experiments with particle injection under rotation, the RB cell is allowed to achieve a steady state at a fixed Ro. Thereafter, particles are injected as the system continues to rotate. Figure 8

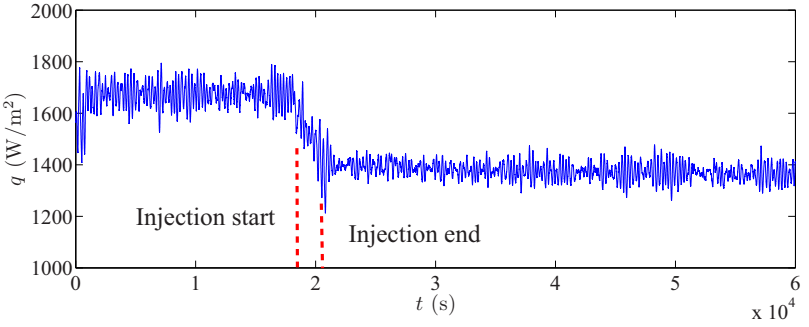

FIG. 8. Variation of heat flux with time during particle injection for run PR2 for particle volume fraction $\phi = 0.22\%$, $\text{Ra}_n = 2.23 \times 10^9$, and $\text{Ro}_n = 0.2$.

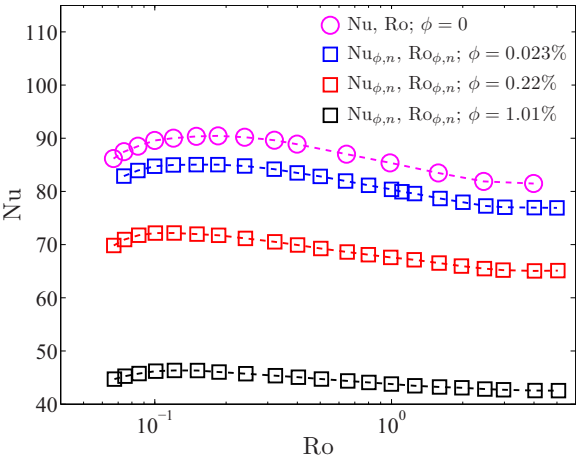

FIG. 9. Variation of $\mathrm{Nu}_{\phi,n}$ with $\mathrm{Ro}_{\phi,n}$ for three particle volume fractions ϕ (runs PR1, PR2, and PR3) and of Nu with Ro for $\phi = 0$ (run nPR3).

shows the variation of input heat flux during such an experiment at $\mathrm{Ra}_n = 2.23 \times 10^9$, $\phi = 0.22\%$, and $\mathrm{Ro}_n = (g\alpha\Delta T/H)^{1/2}/2\Omega = 0.196$. Similar to the case without rotation, q starts decreasing immediately following the commencement of injection, as particles settle on the horizontal surfaces. However, the period of decay, approximately 1.5 h, is significantly shorter than that without rotation (see Fig. 2). Faster settling of the particles can be a result of the damping of the turbulence by rotation. However, it should also be noted that the Ekman pumping mechanism is not able to efficiently resuspend the particles. The smallest thickness of the Ekman boundary layer in the present study is $\delta_E = 2.284\sqrt{\nu/\Omega} \approx 1.5$ mm [40] at $\Omega = 2.05$ rad/s, which is substantially larger than the average particle diameter (100 μm). The increased vertical transport, which is predominantly encountered in the outer region of the Ekman boundary layer [41], is not effective in the resuspension of the particles close to the wall. The nominal Nusselt number, or the heat flux, in the steady state is 18.6% lower than that before injection. Thus the substantial decrease in Nu_n (or q) with relatively small particle volume fraction is similar to that observed in the nonrotating case.

Injections have been carried out for three particle volume fractions $\phi = 0.023\%$, 0.22%, and 1.01% at the same $\mathrm{Ra}_n \approx 2.2 \times 10^9$ and $\mathrm{Ro}_n \approx 0.2$. As with the nonrotating cases, for a given ϕ, reinjection is not performed to measure data at different Ro. Figure 9 shows the variation of $\mathrm{Nu}_{\phi,n}$ with $\mathrm{Ro}_{\phi,n}$ for different ϕ. Data without particles for the same nominal Ra are also included for comparison. The overall trends for $\mathrm{Nu}_{\phi,n}$ are similar to those for $\mathrm{Nu}(\phi = 0)$: an increase in $\mathrm{Nu}_{\phi,n}$ with decreasing $\mathrm{Ro}_{\phi,n}$ setting in at a critical $\mathrm{Ro}_{\phi,n} \approx 2.5$, and a further decay for $\mathrm{Ro}_{\phi,n} \lesssim 0.15$. Thus, the qualitative nature of the heat transfer variation in the different flow regimes seems to be unaffected. However, it is clear that for all rotation rates, the nominal Nu with particles is lower than that without and that the reduction in the nominal Nusselt number increases with increasing ϕ. As expected, the thicker particle layers offer more resistance to the heat transfer as ϕ increases.

Similar to the analysis presented in the previous section, we estimate and account for the temperature drop across the particle layers in order to compare the results with particles to those without.

(i) For each ϕ, we estimate λ_{layer} using Eqs. (8) and (9) and the measurements at $\mathrm{Ro} = \infty$ ($\mathrm{Ra}_n = 2.2 \times 10^9$ in runs PnR1, PnR3, and PnR4) as discussed in Sec. III A. We assume that the conductivity of the particle layers does not vary under rotation. Thus, $\delta T(\mathrm{Ro}_{\phi,n}) = q(\mathrm{Ro}_{\phi,n})e/\lambda_{\mathrm{layer}}$ and hence Ra_ϕ, Ro_ϕ, and Nu_ϕ can be determined for different rotation rates using the measured values of q.

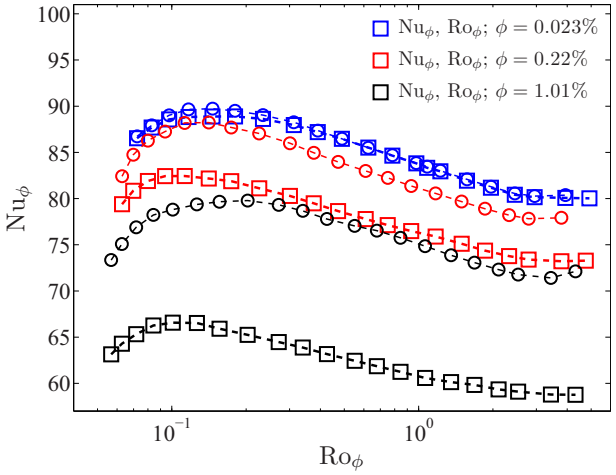

FIG. 10. Variation of Nu_ϕ with Ro_ϕ (squares) for three particle volume fractions ϕ (runs PR1, PR2, and PR3). Circles of the corresponding colors represent $\mathrm{Nu}(\mathrm{Ra}_\phi,\mathrm{Ro}_\phi)$, which is obtained using interpolation of the Nu(Ra,Ro) data from runs nPR1, nPR2, and nPR3 (see Fig. 7), as explained earlier in this section.

(ii) For each ϕ, due to the temperature drop across the particle layers, the values of Ra_ϕ are lower than $\mathrm{Ra}_{\phi,n} \approx 2.2 \times 10^9$ and vary with $\mathrm{Ro}_{\phi,n}$ (since q, and thus δT, varies with $\mathrm{Ro}_{\phi,n}$). For the runs PR1, PR2, and PR3, $\mathrm{Ra}_\phi = (2.08\text{–}2.12) \times 10^9$, $(1.91\text{–}1.95) \times 10^9$, and $(1.39\text{–}1.46) \times 10^9$, respectively. Furthermore, $\mathrm{Ro}_\phi \neq \mathrm{Ro}_{\phi,n}$. In order to compare Nu_ϕ values to those of Nu at the same Rayleigh and Rossby numbers, we estimate $\mathrm{Nu}(\mathrm{Ra}_\phi,\mathrm{Ro}_\phi)$ by interpolation of the Nu(Ra,Ro) data shown in Fig. 7 using spline interpolation.

Figure 10 shows the variation of Nu_ϕ with Ro_ϕ for the three particle volume fractions. Also shown is the reference data for $\phi = 0$, corresponding to the $(\mathrm{Ra}_\phi,\mathrm{Ro}_\phi)$ for each ϕ. It is clear that the differences between the curves for $\phi \neq 0$ and the corresponding curves for $\phi = 0$ in Fig. 10 are significantly smaller than those in Fig. 9. Furthermore, the differences in Fig. 10 are larger at low rotation rates and decrease as Ro_ϕ decreases. Thus, the deterioration in heat transfer due to the particle layers becomes weaker at high rotation rates.

Figure 11 shows the same data, normalized by the respective Nu values at $\mathrm{Ro} = \infty$. For all $\phi \neq 0$, the $\mathrm{Nu}_\phi/\mathrm{Nu}_\phi(\mathrm{Ro}_\phi = \infty)$ follow the corresponding $\mathrm{Nu}/\mathrm{Nu}(\mathrm{Ro} = \infty)$ for $\phi = 0$ up to $\mathrm{Ro}_\phi \gtrsim 0.2$, i.e., in regimes I and II. However, at higher rotation rates, the normalized Nusselt numbers with particle layers become larger than those without and show a delay in transition to regime III in the presence of the particle layers. This delay, indicated by the difference in the locations of the maxima (see the horizontal arrows in Fig. 11), increases with ϕ for low ϕ, before saturating at higher ϕ values. Figure 12 shows the fractional deviation of $\mathrm{Nu}_\phi/\mathrm{Nu}_\phi(\mathrm{Ro}_\phi = \infty)$ from the nonparticle cases, $\Delta\mathrm{Nu}_\phi = \{\mathrm{Nu}_\phi/\mathrm{Nu}_\phi(\mathrm{Ro}_\phi = \infty) - \mathrm{Nu}/\mathrm{Nu}(\mathrm{Ro} = \infty)\}/\{\mathrm{Nu}/\mathrm{Nu}(\mathrm{Ro} = \infty)\}$, as a function of Ro_ϕ for different ϕ. The $\Delta\mathrm{Nu}_\phi$ values deviate significantly from zero only in regime III, where they increase with decreasing Ro. The data also show a weak trend of slightly negative values of $\Delta\mathrm{Nu}_\phi$ for $0.2 \lesssim \mathrm{Ro}_\phi \lesssim 1$, but these deviations are very small. Furthermore, it seems that $\Delta\mathrm{Nu}_\phi$ does not increase linearly with ϕ in regime III and saturates at large ϕ. To further substantiate these observations, we repeat (Sec. III A) that the values of Ra_ϕ and Nu_ϕ are insensitive to the uncertainty in the measured e (or the estimate of λ_{layer}) as it hardly affects $\delta T = qe/\lambda_{\mathrm{layer}}$. Thus, the observation of a delayed transition to regime III and a higher normalized Nu in that regime in the presence of particle layers is not expected to be sensitive to the uncertainty in the thermal properties of the particle layers.

In summary, the results of Secs. III A and III B show that near-neutrally-buoyant particles injected into a statistically steady convective flow (rotating or nonrotating) start separating out from the fluid

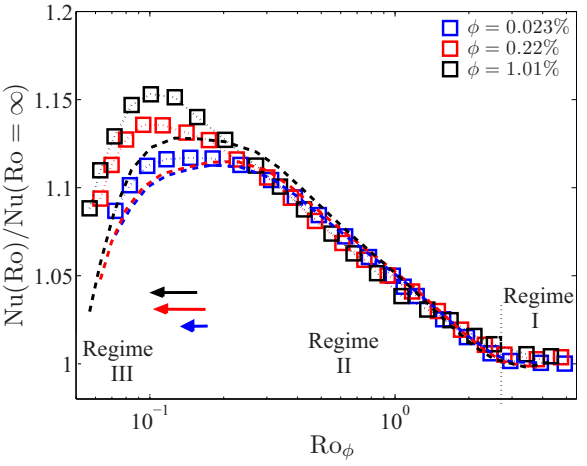

FIG. 11. Variation of $\mathrm{Nu}_\phi/\mathrm{Nu}_\phi(\mathrm{Ro}=\infty)$ with Ro_ϕ (squares) for different particle volume fraction ϕ (runs PR1, PR2, and PR3). Data for $\phi = 0$ for Ra_ϕ corresponding to the $\phi \neq 0$ data are also shown by dashed curves of the corresponding colors without symbols. The black dotted vertical line denotes the approximate location of transition from regime I to regime II, which is the same for all the data sets. The delay in transition from regime II to regime III for different $\phi \neq 0$ in comparison to the corresponding $\phi = 0$ cases is indicated by the horizontal arrows of the corresponding colors.

immediately following injection. The settling process is more rapid under rotation, presumably because of a less turbulent flow. It is apparent that the Ekman pumping mechanism does not aid significantly in the resuspension of the particles entering the boundary layers. As a result, the particles

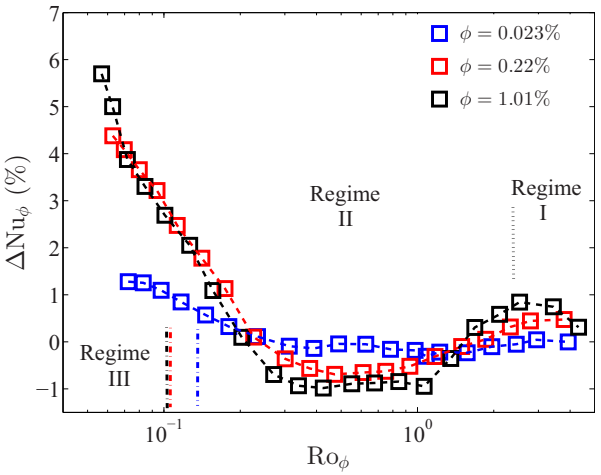

FIG. 12. Variation of $\Delta\mathrm{Nu}_\phi = \{\mathrm{Nu}_\phi/\mathrm{Nu}_\phi(\mathrm{Ro}_\phi=\infty) - \mathrm{Nu}/\mathrm{Nu}(\mathrm{Ro}=\infty)\}/\{\mathrm{Nu}/\mathrm{Nu}(\mathrm{Ro}=\infty)\}$ with Ro_ϕ for different particle volume fraction ϕ (runs PR1, PR2, and PR3). Regimes labeled I, II, and III are the same as those described in the Introduction and indicated in Figs. 7 and 11: regime I characterized by the LSC and negligible effect of rotation, regime II marked by columnar plumes and increasing Nu with decreasing Ro, and regime III with rotation-damped turbulence and suppression of heat transfer. The black dotted vertical line denotes the approximate location of transition from regime I to regime II, which is the same for all the data sets. The different colors of the vertical dash-dotted lines indicating the new locations of the delayed transition between regimes II and III correspond to the respective values of ϕ.

gradually separate out of the fluid and settle on the top and bottom walls, forming particle layers. This process is accompanied by a decrease in the heat flux, which reaches a new statistically steady value when most of the particles have settled on the surfaces. Under nonrotating conditions, the presence of particles at the horizontal walls hinders the heat transfer since $\lambda_{\text{layer}} \ll \lambda_{\text{copper}}$. This degradation in Nu becomes stronger with increasing Ra and ϕ. The particle layers also decrease the heat flux under rotating conditions and do not affect the transition from regime I to II. Specifically, the critical Rossby number for the onset of increase in Nusselt number, i.e., $\text{Ro}_c \approx 2.5$ [7], remains unchanged. However, the peak in $\text{Nu}_\phi/\text{Nu}_\phi(\text{Ro}_\phi = \infty)$, assumed to indicate the transition to the geostrophic regime, is delayed to lower Ro. Furthermore, the reduction in Nu due to the presence of the particle layers is weaker in the geostrophic regime (Fig. 10). As a result, the normalized Nusselt number $\text{Nu}_\phi/\text{Nu}_\phi(\text{Ro}_\phi = \infty)$ shows a positive deviation from the $\phi = 0$ values at high rotation rates (Fig. 11). This deviation increases with increasing particle volume fraction and decreasing Ro (Fig. 12).

IV. DISCUSSION

There have been a few previous studies on the effect of walls of finite conductivity on the heat transfer in RBC, e.g., [35,36,42]. They have shown that Nu decreases as the thermal resistance ($\sim e/\lambda_{\text{wall}}$, where λ_{wall} is the thermal conductivity of the wall) of the walls increases in comparison to that of the fluid and the effects are more pronounced at high Ra as the fluid thermal resistance becomes small. These findings are in agreement with the present observations for nonrotating RBC in the presence of particle layers that have nonideal thermal properties (see Fig. 6). However, the effect of the particle layers leads to a smaller reduction of Nu in the geostrophic regime, which is manifested as a positive deviation from $\text{Nu}/\text{Nu}(\text{Ro} = \infty)$ for $\phi = 0$ (Figs. 11 and 12).

One approach to explain the decrease in Nu in the presence of nonideal walls is to compare the response time of the wall or the particle layer ($\tau_{\text{layer}} \sim e^2/\kappa_{\text{layer}}$) to the characteristic time scale of the flow τ_f [35]. If $\tau_{\text{layer}} \ll \tau_f$, i.e., the thermal response of the wall is rapid enough, the wall is able to maintain an approximately constant surface temperature in response to fluid temperature fluctuations. However, as τ_{layer} becomes comparable to τ_f, the wall is not able to supply the heat demanded by the fluid, e.g., in the case of a rising plume, resulting in the disruption of plume generation and inefficient heat transport. This dependence of heat transport on the relative magnitudes of τ_f and τ_{layer} suggests that for similar wall properties, i.e., similar τ_{layer}, a flow with larger τ_f will experience a smaller deterioration in heat transfer than that for a flow with smaller τ_f. To estimate the flow time scales for different rotation rates, we have performed direct numerical simulations (DNSs) of RB convection in a cell with $\Gamma = 1$ at $\text{Ra} = 1.28 \times 10^9$, $\text{Pr} = 6.7$, and $0.03 \leqslant \text{Ro} \leqslant \infty$. The details about the code have been reported in Ref. [43]. We have performed the simulations with ideal isothermal horizontal walls since the DNS code cannot simulate the thermal dynamics in the interior of a nonideal wall. The simulated system will thus differ somewhat from that with nonideal walls. As such, we use the DNS results only to provide an indication of the trends and relevance of different flow phenomena.

Figures 13 and 14 show the compensated spectra of temperature fluctuations ωE_{TT} at the RB cell center and the thermal boundary layer edge, respectively, for different Ro. Here ω is the angular frequency and E_{TT} is the Fourier transform of the temporal autocorrelation of temperature fluctuations. When ωE_{TT} is plotted on a logarithmic abscissa, equal areas under a curve represent equal contributions to the variance of temperature $\langle T'T' \rangle$, where T' is the temperature fluctuation. The estimate for the characteristic frequency scale of the particle layer for run PR3 ($\phi = 1.01\%$), $\omega_{\text{layer}} = 2\pi/\tau_{\text{layer}} = 2\pi/(e^2/\kappa_{\text{layer}})$, calculated using e and κ_{layer} provided in Table I, is also indicated by the vertical dashed line.[1] It is evident that as the rotation rate increases, the large-time-scale fluctuations become more energetic in comparison to the small-time-scale fluctuations, both in the

[1]Note that, as discussed in Sec. III A, the ratio e/λ_{layer}, and hence $\delta T = q(e/\lambda_{\text{layer}})$, is not sensitive to the uncertainty in e. However, the uncertainty in $\tau_{\text{layer}} = \rho_{\text{layer}} c_{p,\text{layer}} e(e/\lambda_{\text{layer}})$ is substantial, $O(50\%)$ for run PR3 with 4-mm-thick particle layers.

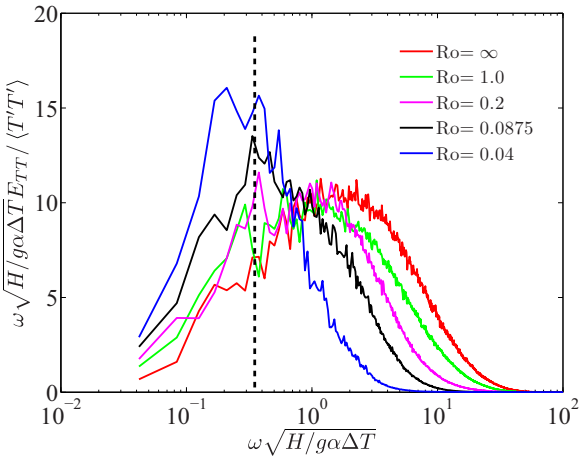

FIG. 13. Compensated spectra of temperature fluctuations at the RB cell center ($0.375 \leqslant z/H \leqslant 0.625$) for different Ro obtained from DNS at $\mathrm{Ra} = 1.28 \times 10^9$ for $\mathrm{Pr} = 6.7$. The vertical dashed line represents $\omega_{\mathrm{layer}}\sqrt{H/g\alpha\Delta T} \approx 0.35$ estimated for the particle layer for the run PR3 with particle volume fraction $\phi = 1.01\%$.

bulk, as well as at the thermal boundary layer edge. This observation is in qualitative agreement with the results of Boubnov and Golitsyn [44] for rotating convection with a free surface at a fixed flux Rayleigh number $\mathrm{Ra}_f = \mathrm{Ra}\,\mathrm{Nu} = 5.1 \times 10^8$ [$\mathrm{Ra} \sim O(10^7)$] and is an indication of the damping effect of rotation on turbulence. However, note that as Ro decreases (from regime I to regime III), the spectra in the bulk of the RB cell gradually move to lower frequencies, whereas at $z = \delta_T$, they do not change substantially until $\mathrm{Ro} \approx 0.2$. Since equal areas under a spectrum represent equal contributions to $\langle T'T'\rangle$, it is also evident that the damping of the small-scale relative to the large-scale fluctuations at high rotation rates is significantly stronger in the bulk than at the boundary layer edge; the blue and black spectra for $\mathrm{Ro} < 0.09$ in Fig. 13 show substantially more energy in the large scales in comparison to those for $\mathrm{Ro} > 0.09$, whereas this trend is weaker in Fig. 14. To

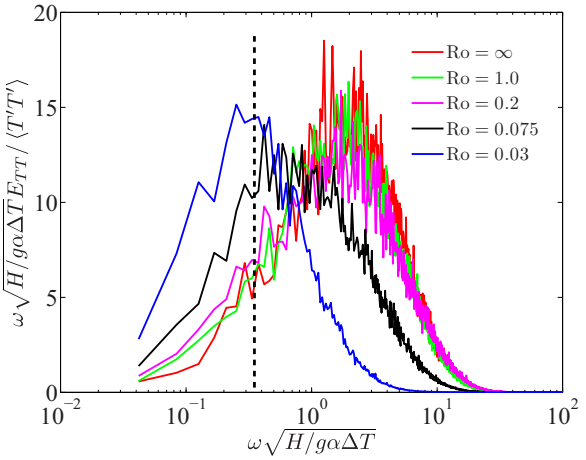

FIG. 14. Compensated spectra of temperature fluctuations at the thermal boundary layer edge for different Ro obtained from DNS at $\mathrm{Ra} = 1.28 \times 10^9$ for $\mathrm{Pr} = 6.7$. The vertical dashed line represents $\omega_{\mathrm{layer}}\sqrt{H/g\alpha\Delta T} \approx 0.35$ estimated for the particle layer for the run PR3 with particle volume fraction $\phi = 1.01\%$.

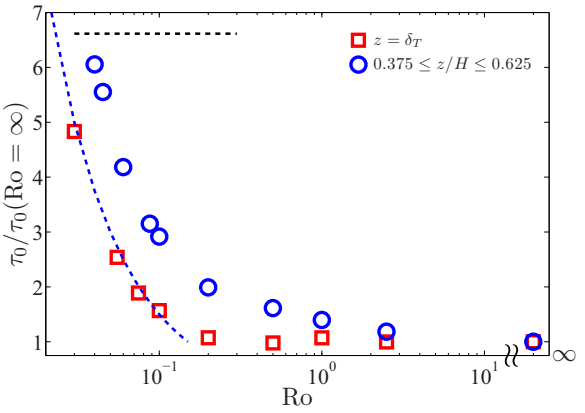

FIG. 15. Variation with Ro of the weighted mean time scale of temperature fluctuations. Here $\mathrm{Ra} = 1.28 \times 10^9$ and $\mathrm{Pr} = 6.7$. The black horizontal dashed line represents $\tau_{\mathrm{layer}}/\tau_0(\mathrm{Ro} = \infty) \approx 6.61$ estimated for the particle layer for the run PR3 with particle volume fraction $\phi = 1.01\%$. The blue dashed curve is $0.15/\mathrm{Ro} \sim \Omega$.

quantify the damping effect, we calculate the weighted mean time scale of temperature fluctuations $\tau_0 = 1/\omega_0 = \int E_{TT} d\omega / \int \omega E_{TT} d\omega$, shown in Fig. 15. Boubnov and Golitsyn [44] found that the representative time scale for the mean spectrum for $\mathrm{Ro} < 1$ measured at a fixed point outside the boundary layer is approximately three times that for $\mathrm{Ro} = \infty$. This observation is in fair agreement with current results presented in Fig. 15. However, as mentioned earlier, we observe important differences between the flow behavior in the bulk and the boundary layers. It is evident that the flow time scales in the bulk start increasing immediately after the transition to regime II and continue to do so as Ro decreases. However, close to the walls, τ_0 remains essentially unchanged until $\mathrm{Ro} \approx 0.2$, although the effect of rotation in the form of Ekman pumping and the associated vortical plumes starts manifesting at $\mathrm{Ro} \approx 2.5$ [26]. It is not until the transition to regime III that the boundary layers show an increase in the time scales. Hence, although rotation is expected to have an overall damping effect on the RB turbulence, it is only in the regime III that the temperature fluctuations in the thermal boundary layer start slowing down. If the overall response of the flow to rotation remains similar in the presence of nonideal walls, the time response of such a wall in relation to the fluid temperature fluctuations close to it can be expected to improve only in the geostrophic regime.

It is important to note that the flow structure in the presence of a nonideal heat transfer wall can be different from that of an ideal surface, as shown by Verzicco [35]. Furthermore, the effect of wall porosity on the dynamics of the Ekman vortices is unknown for the particle layers in the present experiments. However, the strong similarity between the trends for the near-wall τ_0 in Fig. 15 and those for $\Delta\mathrm{Nu}_\phi$ for $\phi = 1.01\%$ in Fig. 12 (i.e., negligible variations in regime II and a rapid increase in regime III) indicates that the overall damping effect of rotation on different regions of the flow is not substantially affected by either the finite thermal diffusivity of the wall or the impact of its porosity on the Ekman vortices. The nearly constant $\tau_0/\tau_0(\mathrm{Ro} = \infty)$ at $z = \delta_T$ for $0.2 \leqslant \mathrm{Ro} \leqslant \infty$ (Fig. 15) indicates that τ_0 close to even an ideal wall is insensitive to the Ekman pumping mechanism, which becomes stronger with decreasing Ro in regime II. Thus, any changes to the Ekman vortices caused by a porous wall may also be expected to have only a minor influence on τ_0 in the boundary layers. Note that in regime III, τ_0 at $z = \delta_T$ seems to scale as Ro^{-1} (blue dashed line in Fig. 15). However, we currently do not have a scaling argument to explain this behavior.

To recapitulate the above discussion, DNS with isothermal heat transfer walls show that the damping effect of rotation on turbulence first manifests in the bulk flow where the time scale of the temperature fluctuations starts increasing as the flow transitions to regime II at $\mathrm{Ro} \approx 2.5$. However, the time scale of the boundary layer temperature fluctuations remains unchanged until the transition to regime III, whereafter τ_0 at $z = \delta_T$ shows an increase with decreasing Ro. Although the

presence of a porous particle layer with nonideal thermal properties may cause the flow structure to deviate from the one with ideal walls, it seems likely that the nature of (and the difference in) the response of the bulk and the boundary layers to rotation persists in the presence of the particle layers. The good agreement between the trends of τ_0 at $z = \delta_T$ obtained from the DNS and those of Nu(Ro)/Nu(Ro $= \infty$) in the presence of the particle layers indeed suggests that the spatially nonuniform response of the flow to rotation does not change qualitatively due to the fluidized particle layers. Thus, $\tau_{\text{layer}}/\tau_f$ is expected to decrease with decreasing Ro only after transition to regime III, consequently improving the time response of the particle layers as experienced by the fluid. As a result, the deterioration in heat transfer due to the finite response time of the particle layers decreases in the geostrophic regime, which shows up as a greater normalized (by its nonrotating value) Nusselt number in comparison to that with ideal walls.

V. SUMMARY

The present study explores the possibility of changing the flow structure and the transitions between the different regimes of RRBC by introducing near-neutrally-buoyant $\sim$100-μm-diam particles at Ra $= 2.2 \times 10^9$, Pr $= 6.4$, and $0.05 \lesssim$ Ro $\leqslant \infty$. For both rotating and nonrotating RBC, particles are injected after the flow has attained equilibrium. The injected particles do not form stable suspensions to enable the assessment of their impact on Nu, but immediately start settling out of the fluid. The system reaches a quasisteady state after 2–5 h when most of the particles have deposited on the horizontal heat transfer walls in the form of porous particle layers. Under system rotation, the injected particles settle out of the fluid faster in comparison to the nonrotating case, as a result of the rotation-damped turbulence in the bulk. It is evident that although the Ekman pumping mechanism increases the vertical velocity fluctuations at the boundary layer edge [7], it is unable to contribute significantly to the resuspension of the settling particles and in turn formation of a stable suspension. Since the thermal conductivity of the particle layers is significantly lower than that of the copper walls, they offer greater thermal resistance and thus decrease the Nusselt number. This decrease in heat transfer can also be viewed as a consequence of the slower response of the particle layers to fluid temperature fluctuations and has been observed before for nonrotating natural convection over nonideal walls [35,36]. Although the behavior of the normalized Nu, i.e., Nu(Ro)/Nu(Ro $= \infty$), remains unchanged in regimes I and II, the particle layers delay the transition to the geostrophic regime III. Furthermore, the normalized Nu in this regime is higher than that with ideal walls and the difference between the two increases with decreasing Ro. Direct numerical simulation results suggest an explanation in terms of a slower time response of the boundary layer fluid in the geostrophic regime relative to the time scale for the particle layers.

ACKNOWLEDGMENTS

This work was supported by the Foundation for Fundamental Research on Matter, Netherlands. The authors gratefully acknowledge support from the Dutch National Science Foundation for the use of supercomputer facilities (Cartesius) under Grants No. SH-202 and No. SH-334.

[1] H. T. Rossby, A study of Bénard convection with and without rotation, J. Fluid Mech. **36**, 309 (1969).

[2] K. Julien, S. Legg, J. McWilliams, and J. Werne, Rapidly rotating turbulent Rayleigh-Bénard convection, J. Fluid Mech. **322**, 243 (1996).

[3] P. Vorobieff and R. E. Ecke, Turbulent rotating convection: an experimental study, J. Fluid Mech. **458**, 191 (2002).

[4] R. P. J. Kunnen, H. J. H. Clercx, and B. J. Geurts, Heat flux intensification by vortical flow localization in rotating convection, Phys. Rev. E **74**, 056306 (2006).

[5] M. Sprague, K. Julien, E. Knobloch, and J. Werne, Numerical simulation of an asymptotically reduced system for rotationally constrained convection, J. Fluid Mech. **551**, 141 (2006).

[6] Y. Liu and R. E. Ecke, Heat transport measurements in turbulent rotating Rayleigh-Bénard convection, Phys. Rev. E **80**, 036314 (2009).
[7] R. J. A. M. Stevens, J.-Q. Zhong, H. J. H. Clercx, G. Ahlers, and D. Lohse, Transitions Between Turbulent States in Rotating Rayleigh-Bénard Convection, Phys. Rev. Lett. **103**, 024503 (2009).
[8] J.-Q. Zhong, R. J. A. M. Stevens, H. J. H. Clercx, R. Verzicco, D. Lohse, and G. Ahlers, Prandtl-, Rayleigh-, and Rossby-Number Dependence of Heat Transport in Turbulent Rotating Rayleigh-Bénard Convection, Phys. Rev. Lett. **102**, 044502 (2009).
[9] R. P. J. Kunnen, B. J. Geurts, and H. J. H. Clercx, Experimental and numerical investigation of turbulent convection in a rotating cylinder, J. Fluid Mech. **642**, 445 (2010).
[10] R. P. J. Kunnen, H. J. H. Clercx, and B. J. Geurts, Vortex statistics in turbulent rotating convection, Phys. Rev. E **82**, 036306 (2010).
[11] J. J. Niemela, S. Babuin, and K. R. Sreenivasan, Turbulent rotating convection at high Rayleigh and Taylor numbers, J. Fluid Mech. **649**, 509 (2010).
[12] S. Schmitz and A. Tilgner, Transitions in turbulent rotating Rayleigh-Bénard convection, Geophys. Astrophys. Fluid Dyn. **104**, 481 (2010).
[13] J.-Q. Zhong and G. Ahlers, Heat transport and the large-scale circulation in rotating turbulent Rayleigh-Bénard convection, J. Fluid Mech. **665**, 300 (2010).
[14] S. Weiss, R. J. A. M. Stevens, J.-Q. Zhong, H. J. H. Clercx, D. Lohse, and G. Ahlers, Finite-Size Effects Lead to Supercritical Bifurcations in Turbulent Rotating Rayleigh-Bénard Convection, Phys. Rev. Lett. **105**, 224501 (2010).
[15] S. Weiss and G. Ahlers, Heat transport by turbulent rotating Rayleigh-Bénard convection and its dependence on the aspect ratio, J. Fluid Mech. **684**, 407 (2011).
[16] R. J. A. M. Stevens, J. Overkamp, D. Lohse, and H. J. H. Clercx, Effect of aspect ratio on vortex distribution and heat transfer in rotating Rayleigh-Bénard convection, Phys. Rev. E **84**, 056313 (2011).
[17] K. Julien, E. Knobloch, A. M. Rubio, and G. M. Vasil, Heat Transport in Low-Rossby-Number Rayleigh-Bénard Convection, Phys. Rev. Lett. **109**, 254503 (2012).
[18] R. J. A. M. Stevens, H. J. H. Clercx, and D. Lohse, Breakdown of the large-scale circulation in $\Gamma = 1/2$ rotating Rayleigh-Bénard flow, Phys. Rev. E **86**, 056311 (2012).
[19] E. M. King, S. Stellmach, and J. M. Aurnou, Heat transfer by rapidly rotating Rayleigh-Bénard convection, J. Fluid Mech. **691**, 568 (2012).
[20] E. M. King, S. Stellmach, and B. Buffett, Scaling behavior in Rayleigh-Bénard convection with and without rotation, J. Fluid Mech. **717**, 449 (2013).
[21] S. Horn and O. Shishkina, Rotating non-Oberbeck-Boussinesq Rayleigh-Bénard convection in water, Phys. Fluids **26**, 055111 (2014).
[22] S. Horn and O. Shishkina, Toroidal and poloidal energy in rotating Rayleigh-Bénard convection, J. Fluid Mech. **762**, 232 (2015).
[23] R. E. Ecke and J. J. Niemela, Heat Transport in the Geostrophic Regime of Rotating Rayleigh-Bénard Convection, Phys. Rev. Lett. **113**, 114301 (2014).
[24] J. Marshall and F. Schott, Open-ocean convection: Observation, theory, and models, Rev. Geophys. **37**, 1 (1999).
[25] J. P. Johnston, Effects of system rotation on turbulence structure: A review relevant to turbomachinery flows, Int. J. Rot. Mach. **4**, 97 (1998).
[26] R. J. A. M. Stevens, H. J. H. Clercx, and D. Lohse, Heat transport and flow structure in rotating Rayleigh-Bénard convection, Eur. J. Mech. B **40**, 41 (2013).
[27] V. Trisaksri and S. Wongwises, Critical review of heat transfer characteristics of nanofluids, Renewable Sustainable Energy Rev. **11**, 512 (2007).
[28] T. Koyaguchi, M. A. Hallworth, H. E. Huppert, and R. S. J. Sparks, Sedimentation of particles from a convecting fluid, Nature (London) **343**, 447 (1990).
[29] M. Okada, C. Kang, K. Oyama, and S. Yano, Natural convection of a water-fine particle suspension in a rectangular cell heated and cooled from opposing vertical walls: The effect of distribution of particle size, Heat Transfer-Asian Res. **30**, 636 (2001).

[30] K. Gotoh, S. Yamada, and T. Nishimura, Influence of thermal convection on particle behavior in solid-liquid suspensions, Adv. Powder Technol. **15**, 499 (2004).
[31] R. P. J. Kunnen, R. J. A. M. Stevens, J. Overkamp, C. Sun, G. F. van Heijst, and H. J. H. Clercx, The role of Stewartson and Ekman layers in turbulent rotating Rayleigh-Bénard convection, J. Fluid Mech. **688**, 422 (2011).
[32] S. Grossmann and D. Lohse, Thermal Convection for Large Prandtl Numbers, Phys. Rev. Lett. **86**, 3316 (2001).
[33] R. J. A. M. Stevens, E. P. van der Poel, S. Grossmann, and D. Lohse, The unifying theory of scaling in thermal convection: The updated prefactors, J. Fluid Mech. **730**, 295 (2013).
[34] Y. Liang, N. Hilal, P. Langston, and V. Starov, Interaction forces between colloidal particles in liquid: Theory and experiment, Adv. Colloid Interface Sci. **134-135**, 151 (2007).
[35] R. Verzicco, Effects of nonperfect thermal sources in turbulent thermal convection, Phys. Fluids **16**, 1965 (2004).
[36] E. Brown, A. Nikolaenko, D. Funfschilling, and G. Ahlers, Heat transport in turbulent Rayleigh-Bénard convection: Effect of finite top- and bottom-plate conductivities, Phys. Fluids **17**, 075108 (2005).
[37] R. W. Powell, C. Y. Ho, and P. E. Liley, *Thermal Conductivity of Selected Materials*, Natl. Stand. Ref. Data Ser., Natl. Bur. Stand. (US) Circ. No. 8 (US GPO, Washington, DC, 1966).
[38] M. D. Shattuck, R. P. Behringer, G. A. Johnson, and J. G. Georgiadis, Onset and Stability of Convection in Porous Media: Visualization by Magnetic Resonance Imaging, Phys. Rev. Lett. **75**, 1934 (1995).
[39] E. Palm, J. E. Weber, and O. Kvernvold, On steady convection in a porous medium, J. Fluid Mech. **54**, 153 (1972).
[40] H. Rajaei, P. Joshi, K. M. J. Alards, R. P. J. Kunnen, F. Toschi, and H. J. H. Clercx, Transitions in turbulent rotating convection: A Lagrangian perspective, Phys. Rev. E **93**, 043129 (2016).
[41] R. J. A. M. Stevens, H. J. H. Clercx, and D. Lohse, Optimal Prandtl number for heat transfer in rotating Rayleigh-Bénard convection, New J. Phys. **12**, 075005 (2010).
[42] J. C. R. Hunt, A. J. Vrieling, F. T. M. Nieuwstadt, and H. J. S. Fernando, The influence of the thermal diffusivity of the lower boundary on eddy motion in convection, J. Fluid Mech. **491**, 183 (2003).
[43] R. Verzicco and R. Camussi, Numerical experiments on strongly turbulent thermal convection in a slender cylindrical cell, J. Fluid Mech. **477**, 19 (2003).
[44] B. M. Boubnov and G. S. Golitsyn, Temperature and velocity field regimes of convective motions in a rotating plane fluid layer, J. Fluid Mech. **219**, 215 (1990).